SAND2017-9142R

Application of Phase-Field Techniques to Hydraulically- and Deformation-Induced Fracture

David Culp, Nathan Miller, and Laura Schweizer

ABSTRACT

Phase-field techniques provide an alternative approach to fracture problems which mitigate some of the computational expense associated with tracking the crack interface and the coalescence of individual fractures. The technique is extended to apply to hydraulically driven fracture such as would occur during fracking or CO_2 sequestration. Additionally, the technique is applied to a stainless steel specimen used in the Sandia Fracture Challenge. It was found that the phase-field model performs very well, at least qualitatively, in both deformation-induced fracture and hydraulically-induced fracture, though spurious hourglassing modes were observed during coupled hydralically-induced fracture. Future work would include performing additional quantitative benchmark tests and updating the model as needed.

Nomenclature

F	=	Deformation Gradient
F^e	=	Elastic part of the deformation gradient
F^p	=	Plastic part of the deformation gradient
$\boldsymbol{b}$	=	Left Cauchy-Green deformation tensor
$\boldsymbol{\sigma}$	=	Cauchy Stress
$\boldsymbol{\tau}$	=	Kirchhoff Stress
Ψ	=	Total Helmholtz Free Energy
$\tilde{\Psi}$	=	Approximate Helmholtz Free Energy
W^+	=	Positive (tensile) strain work
W^-	=	Negative (compressive) strain work
W^p	=	Plastic work
$\overline{W}$	=	Deviatoric work
U	=	Volumetric energy
$\mathcal{H}$	=	Maximum elastic energy
Γ^0	=	Fracture surface
$\mathcal{G}_c^0$	=	Critical fracture energy
K_{eff}	=	Intrinsic Permeability
K_F	=	Fracture Permeability
κ	=	Bulk modulus
μ	=	Shear modulus
Γ^c	=	Damage functional
l_0	=	Fracture length scale
β_e	=	Contribution of elastic work to damage
β_p	=	Contribution of plastic work to damage
c	=	Phase-field variable
$g,\ g_p$	=	Damage functions
f	=	Yield function
k	=	Hardening function
α	=	Hardening state variable
γ	=	Strain-like plastic strain state variable
Φ	=	Tri-axiality function
C_r	=	Reaction coefficient
C_d	=	Diffusion coefficient
C_s	=	Source term
$\langle\cdot\rangle$	=	Macaulay brackets

1 Introduction

1.1 Motivation

The field specific application of fracture mechanics is an increasingly important topic in fields including geophysics, materials engineering, structural mechanics and engineering design. Because fracture is a failure mode that occurs on many scales, both temporally as well as spatially, the ability to enlist the help of parallel computation through finite element simulations is important in predicting and modeling these scenarios. Quantifiable measures of failure, such as damage to a material, can be computed and tracked when running such simulations. These quantities are not directly measureable in experiments, nor are their time-scales reasonable for experimentation, often spanning tens of thousands of years.

Within this paper, a brief overview of the physical processes of interest in fracture are discussed, followed by a summary of a few methods that are often used to predict fracture. An in-depth review of the phase-field method is discussed in Chapter 2 to familiarize the audience with this model and to highlight the loose two-way coupling of the two processes. Chapter 3 presents the numerical tests and their results. Chapter 4 details an extension of the linear-elastic phase-field model to a model that incorporates plasticity. An overview of the continuum-mechanics-based formulation of the model prepares the way for a description of the simulations that have been conducted. A background and discussion of the model's performance on the Sandia Fracture Challenge are also discussed in Chapter 4. Final conclusions are presented in Chaper 5.

1.2 Modeling Fracture Within Solids

The importance of understanding damage evolution has led to the development of numerous fracture models, many of which rely on Griffith's theory for brittle fracture, which relates crack nucleation and propagation to a critical energy release

rate. Theoretical fracture models depend on a crack developing or propagating when this critical value is reached, leading to a process zone that transitions from completely undamaged to fully damaged at a single point [1] or over a specified region [2].

There are various approaches to numerical modeling of fractures within solids. Of these approaches, several are robust in modeling different fracture scenarios, with reasonable computational expense. The extended finite element method (XFEM) enriches the finite element solution space with discontinuous fields associated with a crack independent of the mesh [3]. However, this approach does not specify the particular physics of fracture initiation and propagation, and implementations in 3D are notoriously difficult due to the complexity of the required computational geometry.

Another approach based on the peridynamic theory assumes that particles within a body interact with each other in a nonlocal sense, within a finite neighborhood. In this model, fracture occurs as forces acting between material points decay to zero based on a predefined threshold, e.g., a critical stretch. The peridynamic equations of motion at a point involve an integral functional of the bond forces in a body. It is a continuum theory, which naturally discretizes as a mesh-free particle method [4]. In this aspect, it is favorable over methods that treat cracks explicitly, because the equations of motion and the constitutive models naturally drive fracture initiation and propagation. The use of a pairwise force function is not the traditional method of representing constitutive relations, making the method inconvenient. It is also an oversimplification to assume that any two particles can be simply related with a single force potential [5].

A Lagrangian finite element model for brittle materials based on cohesive zones (CZM) was developed in the mid 1990s. This method is used to predict the propagation of discontinuities along the interface between elements based on a cohesive traction separation law. These models are a departure from brittle fracture, because cracks may develop from the gradual delamination of the crack surfaces. This process takes place in the cohesive zone, which represents an extended crack tip, and was originally formulated to avoid the crack tip stress singularity that is present in linear elastic fracture mechanics. A major advantage of the CZM over linear elastic fracture mechanics is the ability to predict behavior of initially undamaged material [6]. A disadvantage to such a method is the mesh-dependency of the fracture path [2].

2 Phase-Field Formulation

2.1 Damage, Diffusion, and Deformation

There are three important mechanical properties that are of interest in many subsurface rock mechanics problems: deformation, diffusion, and damage. In poroelastic media, these properties are all connected by constitutive relations through the underlying physics. Poroelasticity describes a porous material, with a solid matrix behaving elastically and interstitial fluids that behave viscously. The solid mechanics in such a medium are described using the constitutive laws of linear elasticity, and the fluid mechanics are described with Darcy's law of fluid transport.

The first pair of coupled properties that we will consider within a poroelastic solid is that of damage with deformation. When a solid is deformed, the effective stress within the solid is changed, so long as the surfaces are restrained to limit rigid body modes. When a portion of that solid has reached a critical threshold called the critical energy release rate, or $\mathcal{G}_c^0$, a crack will propagate. Conversely when a fracture forms, the elastic strain energy is relaxed, which alters the displacement field of the solid. This coupled model of damage and deformation is formulated here in terms of a damage variable called phase-field.

Using Biot's linear theory of poroelasticity, the processes of fluid flow and fracture within a material can be coupled: the existence of cracks leads to fluid flowing along these joints known as Poiseuille flow, and conversely, an increased pore pressure, often due to fluid flow, may lead to initiation and/or further propagation of cracks [7].

It is also important to recognize the coupled mechanisms of fluid transport and displacement within a poroelastic medium, which has already been well established by Terzaghi and Biot in the 20th century [8]. An example of this coupling is the increased resistance to deformation of a saturated porous rock as compared to an identical material but subjected to a drained boundary condition. Biot's model of poroelasticty readily demonstrates the diffusion and solid displacement.

2.2 Phase-Field Model of Fracture

In order to better deal with some of the aforementioned challenges, a phase-field model of fracture is considered, whose basic motivation is to smooth out the crack surface discontinuity by using a diffusive scalar field, c. Figure 1 depicts how a variable, c, approximates a discontinuous function (the crack surface in this case). Since the crack is a natural outcome of the analysis, it does not require an explicit geometric representation and tracking, which is an advantage over alternative techniques. This phase-field variable represents damage, and provides a diffuse transition between unbroken and broken material [9]. This damage variable is only defined in the set $[0, 1]$ and will take the value of 0 on the crack surface, while taking a value of 1 away from the crack.

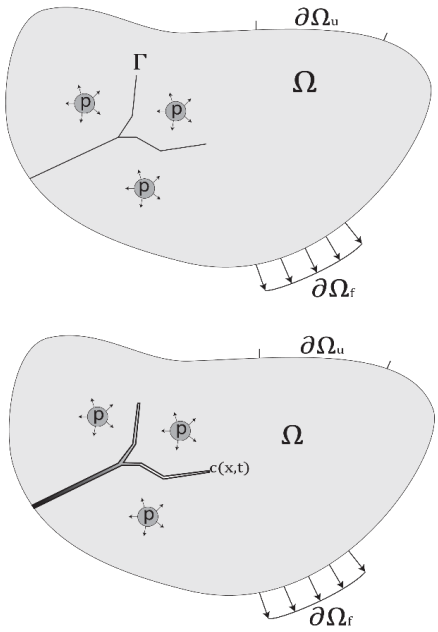

Fig. 1. A diagram representing a solid body Ω, under traction and displacement boundary conditions, $\partial\Omega_f$ and $\partial\Omega_u$ respectively, with crack surfaces represented as Γ, on the left while the phase-field approximation is represented as $c(x,t)$ on the right. Pore pressure, p, is included as a driving force.

2.3 Mathematical Formulation of Linear Elastic Model

We will consider the phase-field formulation which is based on a variational statement of brittle fracture. To do this, we first establish the potential energy of the system. For a linear-elastic, isotropic material, we consider the elastic strain energy density, $\psi_e(\varepsilon)$, where ε is the infinitesimal strain tensor, and both λ and μ are the Lamé coefficients, as shown below in equation (1).

$$\psi_e(\varepsilon) = \frac{1}{2}\lambda\varepsilon_{ii}\varepsilon_{jj} + \mu\varepsilon_{ij}\varepsilon_{ij} \tag{1}$$

In equation (2), the total potential energy, $\Psi(\varepsilon,\Gamma)$, is considered, which is the sum of the elastic strain energy and fracture energy. $\Gamma(t)$ represents a set of crack surfaces that exists within the body at some time t, while Ω is an arbitrary bounded domain [10]. See Figure 1 for a visual representation of the arbitrary, bounded domain. The fracture energy is calculated by integrating $\mathcal{G}_c$, the critical fracture energy, over the entire crack surface Γ [10].

$$\Psi(\varepsilon,\Gamma) = \int_\Omega d\Omega + \int_\Gamma G_c d\Gamma \tag{2}$$

It is convenient to introduce a scalar variable, which we will call the phase-field variable c, to develop a regularized formulation of the total potential energy above. We approximate the fracture energy as a volume integral, rather than a surface integral, and can approximate the fracture energy with an integral of crack density function, Γ_l, which is the integrand in (3) below [11].

$$\Gamma_{l_0}(c) = \int_\Omega \frac{1}{4l_0}[(c-1)^2 + 4l_0|\nabla c|^2]d\Omega \tag{3}$$

A user-chosen length-scale variable, l_0, is introduced which will drive the width over which a fracture is modeled going from $c = 0$ to $c = 1$. It is important to note the aforementioned convention being used for damage, c, in this work. In other

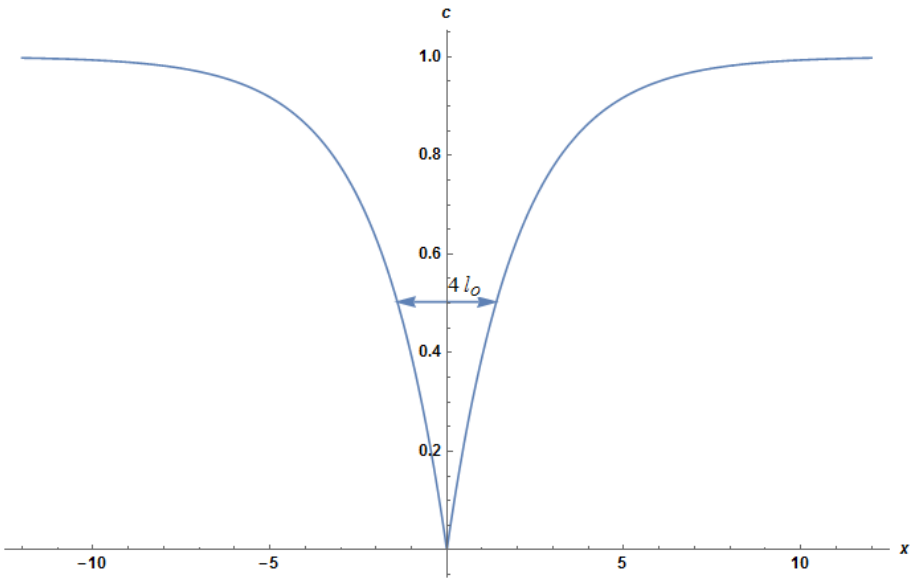

Fig. 2. Phase-field approximation of a crack in 1-D. The damage parameter, c, portrays a fully damaged material at a value of zero, and is spatially smooth moving away from the crack. The length scale, l_0, defines the width over which the crack is smeared

literature, [11] the reverse convention is used. Figure 2.2 depicts how this scalar variable is distributed around a crack with a given length scale. [1] show that equation (3) can be minimized, when the following Euler-Lagrange equation holds true [10]:

$$c - 1 - 4l_0^2 \Delta c = 0 \tag{4}$$

In the case of one dimension, the solution of the differential equation (4) leads to the minimization in a single dimension, x:

$$c(x) = 1 - e^{-|x|/2l_0} \tag{5}$$

which is depicted in Figure 2.

The approximation of equation (2) is finalized by considering the form of the elastic strain energy density function, $\tilde{\psi}(\varepsilon, \Gamma)$. Using Miehe et al. [11] as a template, we decompose ψ_e into the tensile and compressive energy contributions, shown as $\psi_e^+(\varepsilon)$ and $\psi_e^-(\varepsilon)$ respectively, and assume that the elastic strain becomes:

$$\tilde{\psi}(\varepsilon, c) = c^2 \psi_e^+(\varepsilon) + \psi_e^-(\varepsilon) \tag{6}$$

This decomposition effectively removes any crack growth due to compressions, which is considered to be a reasonable assumption for fractures, leaving hydrostatic tension and shear as the sole sources of damage. Finally, we can consider our total potential energy approximation, $\tilde{\Psi}$:

$$\tilde{\Psi}(\varepsilon, c) = \int_\Omega \left[c^2 \psi_e^+(\varepsilon) + \psi_e^-(\varepsilon) + \tfrac{1}{4l_0} \mathcal{G}_c [(1-c)^2 + 4l_0 |\nabla_c|^2] \right] d\Omega \tag{7}$$

In order to impose the irreversible nature of crack growth into our model, a strain-history field, $\mathcal{H}$, is introduced which satisfies the Kuhn-Tucker conditions for loading and unloading and will replace the tensile contribution of strain energy, ψ_e^+, when solving for the damage variable. This replacement addresses the idea that c is a monotonically decreasing parameter, and a damaged material will not heal under compressive stresses. This is expressed in equation (8):

$$\frac{\partial c}{\partial t} \geq 0 \tag{8}$$

Now let us consider the kinetic energy of this arbitrary body:

$$\Psi_{kin}(\dot{u}) = \frac{1}{2}\int_{\Omega} \rho \dot{u}_i \dot{u}_i d\Omega, \tag{9}$$

where $\dot{u} = \frac{\partial u}{\partial t}$ is the velocity of the body, and ρ is its mass-density. Now that we have formulated the potential and kinetic energies of the body, we are able to form the Lagrangian of the fracture problem from (7) and (9):

$$\mathcal{L}(\dot{u}, u, \Gamma) = \Psi_{kin} - \Psi_{pot} = \frac{1}{2}\int_{\Omega} \rho \dot{u}_i \dot{u}_i d\Omega - \int_{\Omega} \left[c^2 \mathcal{H}(\varepsilon) + \psi_e^-(\varepsilon) + \frac{1}{4l_0}\mathcal{G}_c[(1-c)^2 + 4l_0|\nabla_c|^2] \right] d\Omega \tag{10}$$

Using the Euler-Lagrange equations, we write the governing partial differential equations that describe the problem at hand, whose solutions are minimizers of the energy functional above:

$$\left(\frac{4l_0 c\mathcal{H}}{\mathcal{G}_c} + 1 \right) c - 4l_0^2 \frac{\partial^2 c}{\partial x_i^2} = 1 \tag{11}$$

$$\frac{\partial \sigma_{ij}}{\partial x_j} = \rho \ddot{u}_i \tag{12}$$

where $\ddot{u}$ represents the second derivative of position with respect to time, i.e. the acceleration. As a broad review of the derivation, (11) and (12) fall out of the Lagrangian energy functional after applying Euler-Lagrange equations [10]. Note that (12) is simply a statement of the conservation of momentum from the classical continuum theory. These equations, which are the strong form equations of motion, can be solved in unison to find the displacement field and phase-field given the following boundary and initial conditions:

$$(BC) \begin{cases} u_i & = g_i \\ \sigma_{ij} n_j & = t_i \\ \frac{\partial c}{\partial x_i} n_i & = 0 \end{cases} \tag{13}$$

$$(IC) \begin{cases} u(\boldsymbol{x}, 0) & = \boldsymbol{u}_0(\boldsymbol{x}) \\ \dot{u}(\boldsymbol{x}, 0) & = \boldsymbol{v}_0(\boldsymbol{x}) \\ c(\boldsymbol{x}, 0) & = c_0(\boldsymbol{x}) \end{cases} \tag{14}$$

2.4 Two-Way Coupling

Rather than considering a bulk approach to the coupling of fluids and solids in poroelastic media, we will consider the two phases separately during each time-step and update these properties with a loose coupling. By implementing the constitutive relations independently of one another, we are able to model the effective stress and stress contribution of the fluid pressure. We do this to take the individual contributions of its solid and fluid constituents into account, preventing the need to lump the states' parameters into one model and lose sensitivity to a change in a material's porosity or fluid content. Because we are considering a two-way coupling between fluid flow and damage, a formulation of how each field is updated is required. Let us first consider how the phase-field variable is modified by the onset of fluid flow with a medium. By solving the Lagrangian system formulated earlier, we are able to compute the damage field within the medium, given a particular

state of stress. When considering a porous, fluid-saturated material, equation (15), is needed to incorporate the hydrostatic pressure of the fluid filling the pore-spaces.

$$\sigma = c^2 \tilde{\sigma_{eff}} - bp, \tag{15}$$

where σ is the total stress, and $\tilde{\sigma_{eff}}$ is the effective stress in the solid skeleton, b is Biot's coefficient, and p is the fluid pore pressure. Including the hydrostatic pressure allows for the flow to directly affect the stress and consequently the damage. We will also allow the permeability to be increased with higher levels of damage completing the coupling.

A joint opening vector is computed as a field variable over the elements in the model using the spatial gradient of the phase-field variable. This state variable will allow the computation of Poiseuille-type flow through cracks and couple the flow to the solid mechanics portion of the simulation. The joint opening state variables can be summarized by the equations below, in which $\lambda_\perp$ represents the stretch perpendicular while ∇c represents the gradient of damage, and $\boldsymbol{C}^{-1}$ is the inverse of the Right-Cauchy Green tensor in (16).

$$\lambda_\perp^2 = \frac{\nabla c \cdot \nabla c}{\nabla c \cdot \boldsymbol{C}^{-1} \cdot \nabla c} \tag{16}$$

$$\omega^2 = \begin{cases} (\lambda_\perp - 1)^2 L_\perp^2 & c < c_0 \\ 0 & otherwise \end{cases} \tag{17}$$

$$\delta_n = \omega \boldsymbol{n} \tag{18}$$

The crack opening width, represented by ω, is formed from a product of the element length in the neighborhood of the crack, $L_\perp$, and an adjusted stretch vector. As (17) indicates, this value is zero unless the damage is greater than some user-chosen threshold value, c_0. Ultimately, the joint opening vector δ_n, the state variable of interest, is formed by scaling the unit vector normal on the deformed crack surface, $\boldsymbol{n}$, by the crack opening as shown in (17). These equations have been modified from [12].

In addition to the Darcy flow within the porous material, we need to also consider the additional fluid mass flux through a fracture, which is achieved by altering the effective permeability of the cracked media. This Poiseuille flow has a a quadratic dependence on ω as shown in (19), where $\bar{\eta}$ is the dynamic viscosity of the fluid, and α is a coefficient based on the distribution of the fractures in the media.

$$K_F = \alpha \frac{1}{12\bar{\eta}} \omega^2 \tag{19}$$

Now we can write:

$$K_{eff} = K_m \boldsymbol{I} + K_F (I - \boldsymbol{nn}), \tag{20}$$

where K_m is the permeability of the matrix, and K_{eff} is the modeled intrinsic permeability [13]. Other approaches exist that make use of the joint opening including [12], in which a continuum mechanics approach is taken, as shown in (21).

$$\hat{\boldsymbol{K}}_{fracture} = K_c \omega^2 J [\boldsymbol{C}^{-1} - (\boldsymbol{C}^{-1} \boldsymbol{n}_0) \otimes (\boldsymbol{C}^{-1} \boldsymbol{n}_0) \tag{21}$$

In this configuration, K_c is similar to K_F in (19), with $\boldsymbol{n}_0$ being the deformation of a line element perpendicular to the material crack surface. From their formulation it follows that

$$\hat{K}(\boldsymbol{F}, d) = K_m(\boldsymbol{f}) + d^{\varepsilon_0} \hat{\boldsymbol{K}}_{fracture}(\boldsymbol{F}), \tag{22}$$

where ε_0 is a material parameter. For the numerical investigations describes in this paper, the approach described in equation (20) was used.

3 Coupled Flow-Fracture Results

3.1 Overview of Numerical Methods

The numerical models in these studies make use of Sierra Mechanics, Shaw et al., 2015, developed at Sandia National Laboratories, which is an engineering mechanics simulation framework that has been developed to study computational mechanics using MPI parallel finite element discretization. A variety of rock mechanics problems can be addressed with this suite of codes, and of particular interest to this work is the solid mechanics module called Adagio, and the fluid mechanics module called Aria. Within Sierra's material library, LAMÉ, a C++ material class called "Phase-field Porous Flow" was created to run simulations for fracture and flow problems, based on a phase-field approach to handle the crack propagation as described above. This material model modifies the standard phase-field model in two critical ways: 1) the total stress is augmented by the hydrostatic term, and 2) the joint opening vector is computed from the phase and which will be used to update a material's permeability. The following sub-sections detail these processes.

Because we would like to solve for displacements and fluid pressures using seperate modules, Sierra has a tool called Arpeggio that handles the transfer of these fields from one solver to another. After initalizing the solid and fluid parameters, a transfer protocol is setup within the input deck, which tells Aria to send the pore pressures to Adagio, which in turn uses the inital pore pressures to update the displacements and phase-field variables in the solid model. After this update occurs, the joint opening variables are passed into a user subroutine, which carries out the operation in equation (20), updating K_{eff}. The newly updated permeability is then passed on to Aria, which computes the flow with this newly updated permeability information. The linear elastic phase-field, along with the displacement field, are solved using an explicit time-staggered integration, utilizing an implicit solver for the parameter c [14].

3.2 Fluid Injection

To test this model, we consider a thin, rectangular domain made of Hex-8 solid elements. The initial time step was chosen to be 0.1 s, although the timestep was allowed to be adaptive in order to converge with larger load-steps. The material parameters were akin to those of an average limestone with $E = 10$ GPa, $\rho = 2250 \frac{kg}{m^3}$, $\nu = 0.155$, $l_0 = 0.25$ m, $\mathcal{G}_c^0 = 98$. The phase-field was initialized to 1 across the entire mesh, and pressures were equally set to zero. A flux boundary condition was imposed upon a single element in the bottom left portion of the mesh, whcih will call the injection zone. A mass flux rate of $5 \frac{kg}{s^2 m^2}$ was imposed, starting with a mass flux of zero at $t = 0$, was the source of damage.

In the first simulation, displacements in both x and y were fixed along both the bottom and left boundaries. This set of boundary conditions prevented displacement, or fluid flow below $x = 0$ and $y = 0$ and in a sense caused a corner condition. We set the fixed displacement conditions as such in order to produce a fracture in a quasi-static loading scenario: without such boundaries, we would observe a symmetric expansion of the injection area, leading to a completely damaged area that grew radially, rather than a fracture. As the fluid pressure builds in the injection area, the critical stress is reached after a few timesteps, and the phase-field variable begins to decrease. As the permeability increases in the damaged areas, portions of the mesh near the corners begin to accumulate higher fluid pressure than those areas not near the boundaries, resulting in two fractures that form and propagate parallel to the fixed boundaries.

As seen below in Figure 3, this demonstrates, qualitatively, that the two-way coupling behaves in a way that seems reasonable. The top left quadrant of the figure shows the phase-field solution at time $t = 8s$, as the fracture has propagated to near the boundary. The top right quadrant shows the computed joint opening magnitudes at the same time, while the bottom left quadrant shows the pore pressures that have spread along the newly formed joint. The final quadrant shows the xx component of intrinsic permeability, which is increased along the fracture. While nearly symmetric, it can be easily observed that this solution is not entirely symmetric. We suspect that this is due to the reduced integration scheme used during the solution scheme.

In a second numerical test, we used the same parameters as described above, but altered the boundary conditions to that of quarter-symmetry. This is achieved by only fixing displacements in the x direction on the left side of the mesh and in the y direction on the bottom side. As additional fluid mass is injected into the injection area, flow and displacements occur parallel to the boundaries, both in the $+x$ and $+y$ directions. We can see in Figure that this is the direction of fracture propagation. This also demonstrates a qualitatively sound solution.

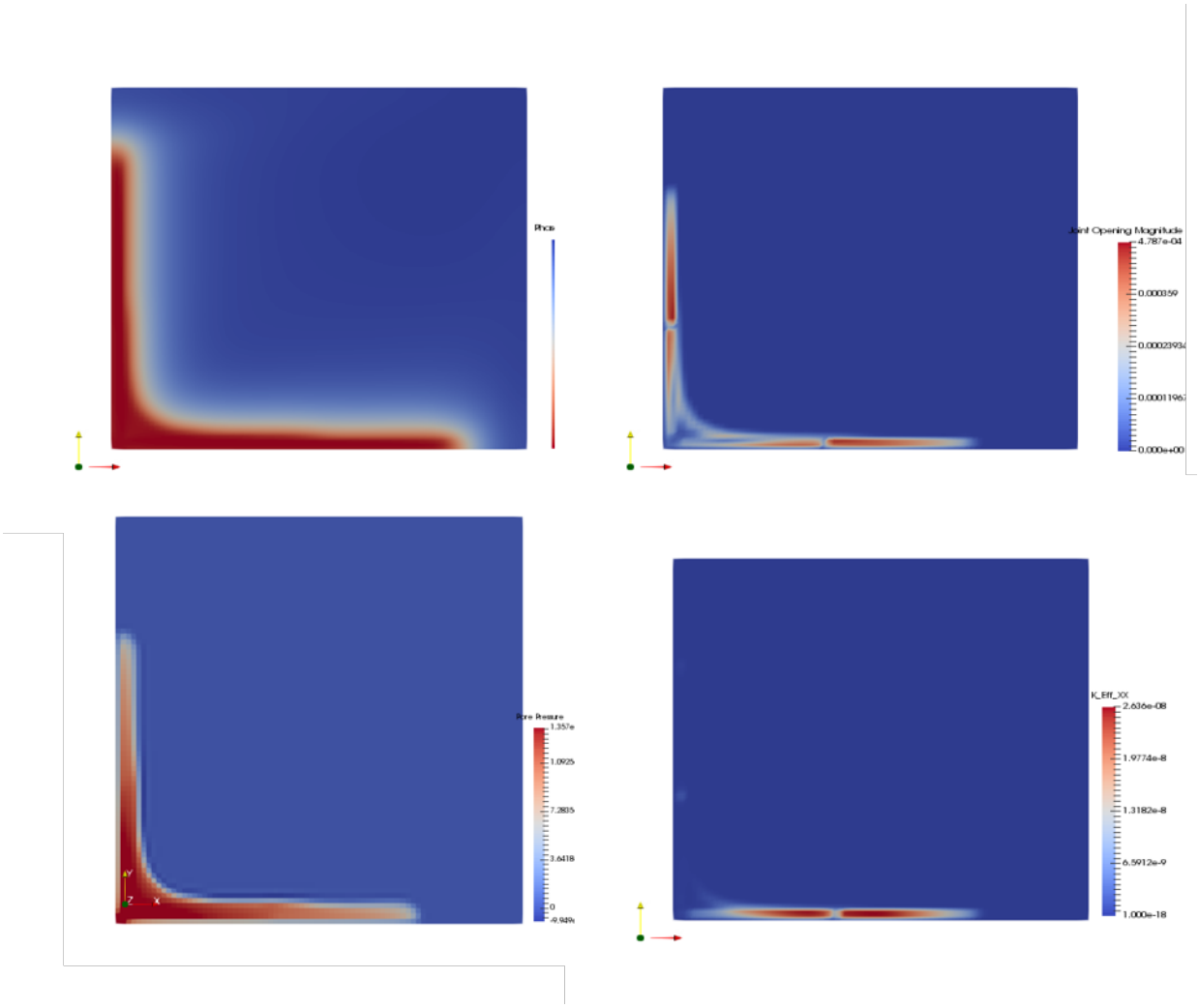

Fig. 3. Variables of interest at time $t = 8$ during the second fluid injection test. From top left clockwise: Phase-field, Joint Opening Magnitude (m), xy component of Effective Permeability Tensor (H/m)
, and Pore Pressure (Pa)

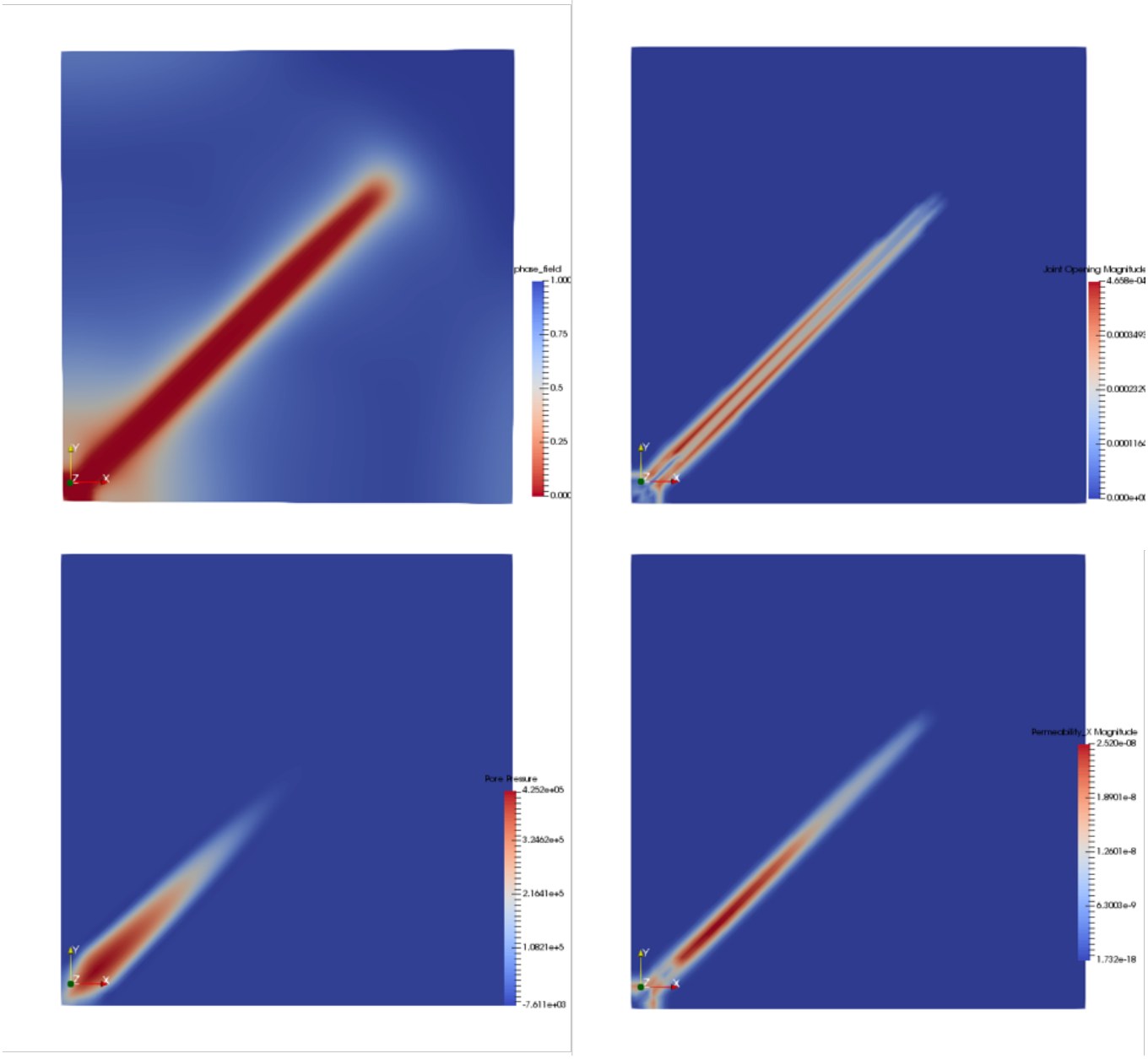

Fig. 4. Variables of interest at time $t = 8$ during the second fluid injection test. From top left clockwise: Phase-field, Joint Opening Magnitude (m), xy component of Effective Permeability Tensor (H/m)
, and Pore Pressure (Pa)

3.3 Hourglass Effects

As previously mentioned, the solutions we encountered were not always symmetric, even when setting up the test with perfect symmetry. Upon closer inspection, it appears that this was due to the use of reduced integration, resulting in spurious hourglass modes. We further suspect that use of incompressible fluids to drive the loading is the reason why the reduced integration is an issue. Figure 5 shows the phase-field solution after several time steps of a fluid volume being injected into a slot. The asymmetries along the corners of the solution, and at edges of the injection zone are obvious. As the simulation continues to run, the onset of a chaotic solution becomes evident, as shown in Figure 6. Because of these spurious modes, we had to avoid certain geometries and loading scenarios for our numerical tests. When comparing this to a similar test of pore-pressure injection in Adagio, using fully integrated elements, such unpleasantries were avoided. Running Arpeggio with fully integrated elements was not within the scope of this project, due to limited time once the issue was discovered. This just goes to show that sometimes it just isn't worth being rank-deficient.

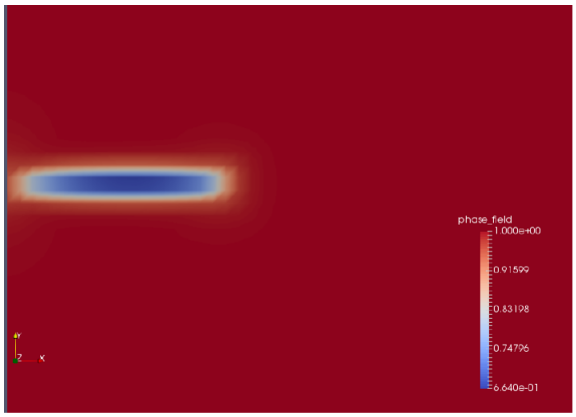

Fig. 5. Upclose view of injection zone as hourglassing effects become evident

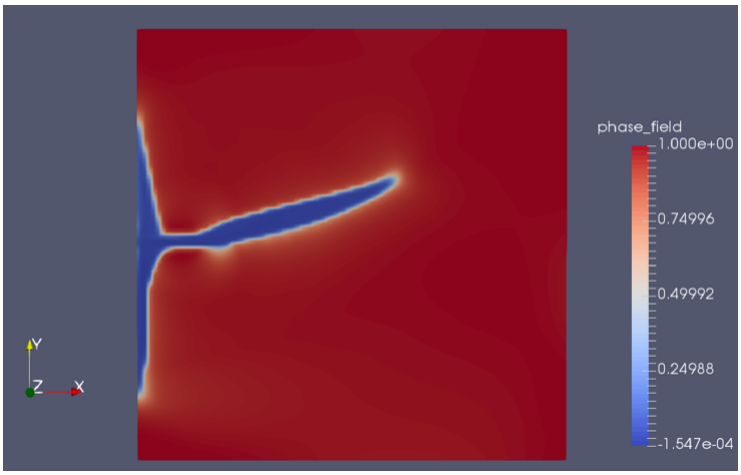

Fig. 6. Results of injection test after onset of hourglass effects

4 Sandia Fracture Challenge

4.1 Background on Sandia Fracture Challenge

In 2010, Sandia National Lab proposed the first Fracture Challenge. The purpose of the challenge was to determine the extent to which members of the fracture mechanics community could accurately model fracture in a relatively simple test scenario. Several samples of a test coupon were created and loaded in tension to failure. The challenge was done in a double-blind fashion; the participants in the challenge had no *a priori* knowledge of the experimental outcomes, while

the experimenters had no knowledge of the modeling methods and results used by the participants. Comparisons of results were made at the end of the challenge period. Model accuracy was determined by comparing crack path, crack opening displacement (COD), and the forces at which the crack developed and propagated to experimental results [15].

The geometry of the test coupon is shown in Figure 7. The geometry was intended to be relatively simple, yet not analytically solvable. Participants were provided with all geometry and specified manufacturing tolerances.

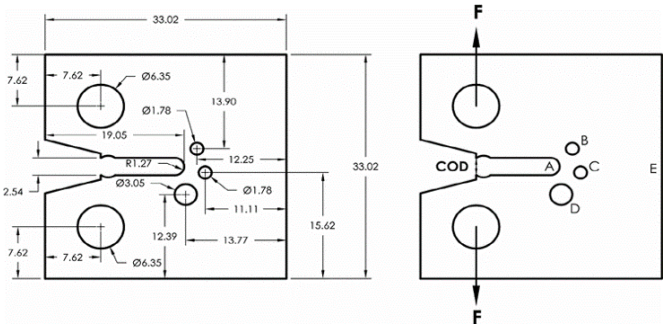

Fig. 7. Geometry of test coupon used in Fracture Challenge. Dimensions are in millimeters.

Sandia also provided participants with detailed material specifications, including alloy composition, heat treatment data, and surface micrographs. The material used was 15-5 PH, a martenistic hardened stainless steel. Four tensile coupons, shown in Figure 8, were taken from the same sheet of material as the fracture challenge coupons and tested to failure. Stress-strain curves (Figure 9) from these tests were provided to participants as well [15].

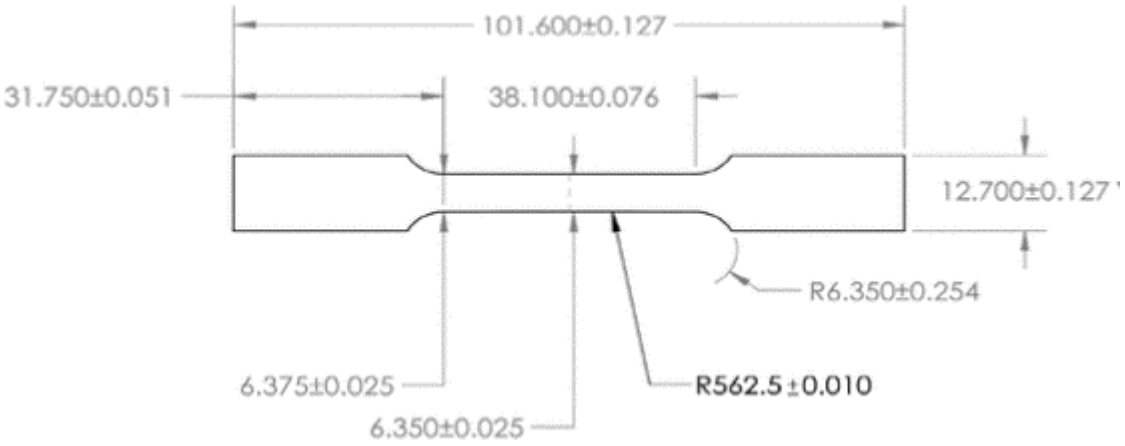

Fig. 8. Geometry of the tensile test coupon

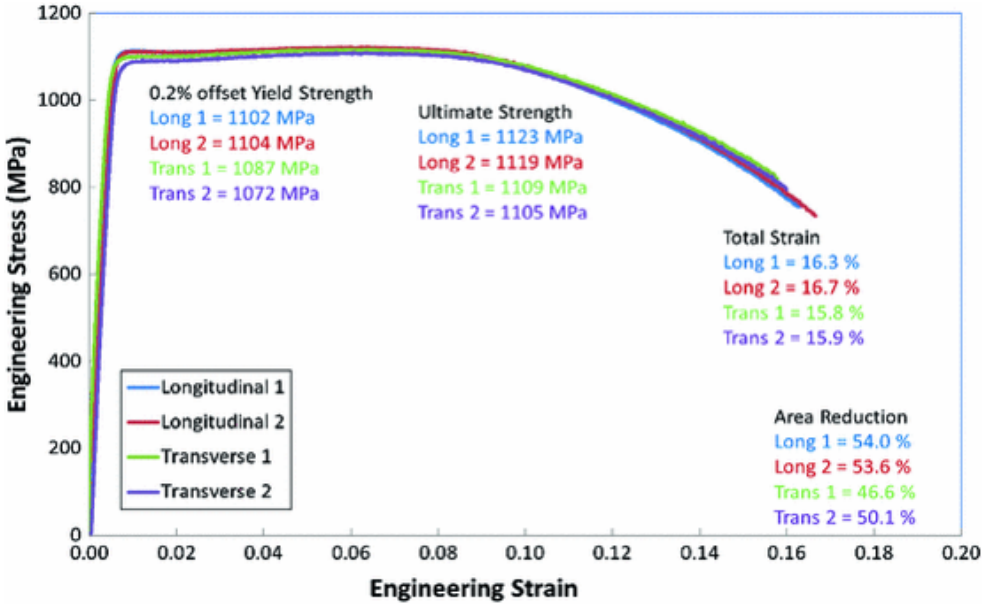

Fig. 9. Results of tensile test obtained by Sandia

4.2 Incorporating Plasticity into the Phase-Field Material Class

The previously described phase-field constitutive model has been shown to be effective in representing the deformation of geo-materials which, in general, display brittle fracture [16]. Briefly, materials which do not display significant amounts of plastic deformation prior to fracture are considered brittle, while those that fracture after the onset of significant amounts of plasticity are considered ductile, such as some metals. Interestingly, metals will exhibit ductile fracture combined with brittle fracture depending both on the material and the load case [17]. From the provided load-displacement curves, it was observed that significant plasticity occurred in the material prior to fracture. For this reason, an equation for ductile materials was sought.

4.3 Phase Field Plasticity Model

The phase field plasticity model implemented was taken from the paper by Borden et. al. [18]. In this paper a J2 flow plasticity model was developed which accounts both for stress tri-axiality as well as the ability for plasticity to continue accruing as damage increases. A brief discussion of the derivation of the fracture model is presented here.

The deformation gradient $\boldsymbol{F}$ is broken down into a plastic portion $\boldsymbol{F}^p$ and an elastic portion $\boldsymbol{F}^e$ as

$$\boldsymbol{F} = \boldsymbol{F}^e \boldsymbol{F}^p$$

The total stored energy can be written as

$$\Psi\left(\boldsymbol{F}, \Gamma^0\right) = \int_{\Omega_0} W(\boldsymbol{F}) d\Omega_0 + \int_{\Gamma^0} \mathcal{G}_c^0 d\Gamma^0$$

The phase-field approximation takes the form

$$\tilde{\Psi}(\boldsymbol{F}, c, \nabla c) = \int_{\Omega} g(c) W(\boldsymbol{F}) dV + \int_{\Gamma^0} \mathcal{G}_c^0 \Gamma^c(c, \nabla c) d\Gamma^0$$

where

$$\Gamma^c(c, \nabla c) = \frac{1}{4 l_0}\left((c-1)^2 + 4 l_0 \nabla c \cdot \nabla c\right)$$

Similarly to the pore pressure approach, cracks are assumed to not effect the energy of hydrostatic compression so the energy is separated into a positive and negative hydrostatic stress. Additionally, the energy dissipation due to plastic work is included. This leads to the total energy being written as

$$\tilde{\Psi}(\boldsymbol{F},c,\nabla c)=\int_{\Omega}\left[g(c)W^{+}(\boldsymbol{F})+W^{-}(\boldsymbol{F})+g_{p}(c)W^{p}(\alpha)\right]dV+\int_{\Gamma^{0}}\mathcal{G}_{c}^{0}\Gamma^{c}(c,\nabla c)\,d\Gamma^{0}$$

where $g_p(c)$ is the damage function for plasticity taken here to be identical to $g(c)$ and α is the state variable which tracks the evolution of plastic strain. Instead of the quadratic form of $g(c)$ used in the pore fluid pressure phase field model, this new approach utilizes a cubic representation of

$$g(c)=s\left(c^{3}-c^{2}\right)+3c^{2}-2c^{3}$$

where s is a parameter which determines the slope of g at $c=1$ and is typically set to $10e-4$. Neglecting the derivation of the governing equations (see Borden [18]) we arrive at the following expression for the phase field model

$$\frac{2l_{0}}{\mathcal{G}_{c}^{0}}\left(\beta_{e}g'(c)\mathcal{H}+\beta_{p}g_{p}'(c)\langle W_{p}-W_{0}\rangle\right)+c-4l_{0}^{2}\nabla c\cdot\nabla c=1$$

This expression will be solved using Sierra's reaction-diffusion equation solver with

$$\begin{aligned}C_{r}&=\frac{2l_{0}}{c\mathcal{G}_{c}^{0}}\left(\beta_{e}g'(c)\mathcal{H}+\beta_{p}g_{p}'(c)\langle W_{p}-W_{0}\rangle\right)+1\\C_{d}&=4l_{0}^{2}\\C_{s}&=1\end{aligned}$$

where C_r is the reaction coefficient, C_d is the diffusion coefficient, and C_s is the source term. The plastic response is a typical J2 flow model with a yield function defined as

$$f=||\boldsymbol{s}||-g_{p}(c)\sqrt{\frac{2}{3}}k(\alpha)$$

where $\boldsymbol{s}$ is the deviatoric part of the Kirchhoff stress i.e. ($\boldsymbol{\tau}=J\boldsymbol{\sigma}$ where $\boldsymbol{\sigma}$ is the Cauchy stress). The flow rule is assumed to be associative leading to

$$\boldsymbol{n}=\frac{\boldsymbol{s}}{||\boldsymbol{s}||}$$

The plastic power is typically defined as

$$\dot{W}^{p}=\dot{\gamma}||\boldsymbol{s}||$$

but in order to include tri-axiality effects from the stress it is defined as

$$\dot{W}^{p}=\dot{\gamma}\frac{||\boldsymbol{s}||}{\phi}$$

where

$$\phi = d_1 + d_2 e^{\frac{d_3 \text{trace}(\boldsymbol{\tau})}{3||\boldsymbol{s}||}}$$

and d_1, d_2, and d_3 are parameters.

The plasticity model is evaluated in the following steps

1. The state variables are extracted (α, $\overline{\boldsymbol{b}}^e_n$)
2. The change in the deformation gradient is assumed to be all elastic and $\overline{\boldsymbol{b}}^e_{n+1} = \Delta\boldsymbol{F}\overline{\boldsymbol{b}}^e_n(\Delta\boldsymbol{F})^T$
3. The deviatoric trial stress is calculated $\boldsymbol{s} = g(c)\mu\text{dev}\left[\overline{\boldsymbol{b}}^e_{n+1}\right]$
4. The yield condition is evaluated $f = ||\boldsymbol{s}|| - g_p(c)\sqrt{\frac{2}{3}}k(\alpha)$
5. If $f <= 0$ then let $\delta\gamma = 0$ and go to (6)
   (a) Define $\overline{I}^{tr}_{b^e} = \frac{1}{3}\text{trace}\left[\overline{\boldsymbol{b}}^e_{n+1}\right]$, $\overline{\mu} = g(c)\mu\overline{I}^{tr}_{b^e}$
   (b) Solve for $\delta\gamma$ using a Newton-Raphson iteration: $||\boldsymbol{s}|| - g_p(c)\sqrt{\frac{2}{3}}k\left(\alpha + \sqrt{\frac{2}{3}}\Delta\gamma\right) - 2\overline{\mu}\Delta\gamma = 0$
   (c) Update $\boldsymbol{s} = \boldsymbol{s} - 2\overline{\mu}\Delta\gamma\boldsymbol{n}$, $\alpha = \alpha + \sqrt{\frac{2}{3}}$
6. Update the Kirchhoff stress $J = \det[\boldsymbol{F}]$
   $U'(J) = \frac{\kappa}{2J}\left(J^2 - 1\right)$
   $p = \begin{cases} g(c)U'(J) & \text{if} J > 1 \\ U'(J) & \text{otherwise} \end{cases}$
7. Update $\overline{\boldsymbol{b}}^e_{n+1}$
   $\overline{\boldsymbol{b}}^e_{n+1} = \frac{\boldsymbol{s}}{g(c)\mu} + \overline{I}_{b^e}\boldsymbol{I}$
   Note that $\overline{I}_{b^e} \neq \overline{I}^{tr}_{b^e}$ and must be solved for using a Newton iteration to ensure $\det\left(\overline{\boldsymbol{b}}^e_{n+1}\right) = 1$.
8. Compute W^+ and update H

$$\begin{aligned}
W^p &= W^p + \Delta\gamma\frac{||\boldsymbol{s}||}{\phi} \\
U^+ &= \begin{cases} \frac{1}{2}\kappa\left(\frac{1}{2}\left(J^2 - 1\right) - \log(J)\right) & \text{if } J > 1 \\ 0 & \text{otherwise} \end{cases} \\
\boldsymbol{b}^e &= J^{\frac{2}{3}}\overline{\boldsymbol{b}}^e_{n+1} \\
\boldsymbol{C}^p &= \boldsymbol{F}^{-1}\boldsymbol{b}^e\boldsymbol{F}^{-T} \\
\overline{W} &= \frac{1}{2}\mu\left(\frac{1}{J^{\frac{2}{3}}}\left(\boldsymbol{F}^T\boldsymbol{F}\right) : (\boldsymbol{C}^p)^{-1} - 3\right) \; (note:)\boldsymbol{A} : \boldsymbol{B} = A_{ij}B_{ij} \\
W^+ &= \overline{W} + U^+ \\
H &= max\left(H, W^+\right)
\end{aligned}$$

9. Update reaction diffusion coefficients

$$\begin{aligned}
l_{factor} &= \frac{1}{l_0^3} \\
C_r &= \left\{\frac{2l_0}{\mathcal{G}_c^0}\left(\beta_e g'(c)\mathcal{H} + \beta_p g'_p(c)\langle W_p - W_0\rangle\right) + c\right\} l_{factor} \\
C_d &= 4l_0^2 l_{factor} \\
C_s &= 1 l_{factor}
\end{aligned}$$

4.4 Model Testing

Once the J2 Flow model was implemented within Sierra, the group performed benchmark testing. The group attempted to replicate the tensile test performed by Sandia, to tune the material properties as well as model parameters such as W_0. The mesh used is shown in Figure 10. This mesh was fixed on the $-x$ end, and a displacement was applied on the $+x$ end at a rate of $1 \times 10^{-3}\ m/s$. Note that both the tensile test simulation and the Fracture Challenge simulation employed adaptive time-stepping, to aid convergence of the reaction-diffusion solver.

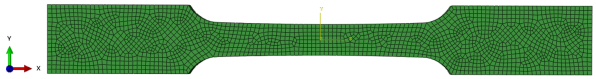

Fig. 10. Mesh of tensile test coupon

The results qualitatively behave as expected for a tensile test specimen. The damage, represented by the phase-field, accurately indicates the region where necking begins. Both plastic strain and plastic work also demonstrate this. These results are shown in Figures 11, 12, and 13, respectively.

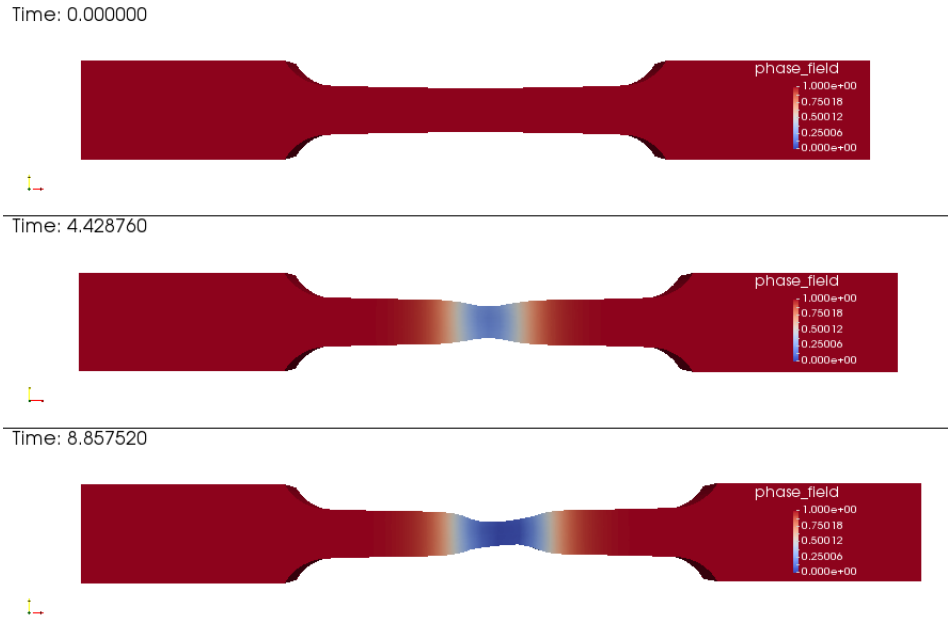

Fig. 11. Phase-Field progression during tensile test

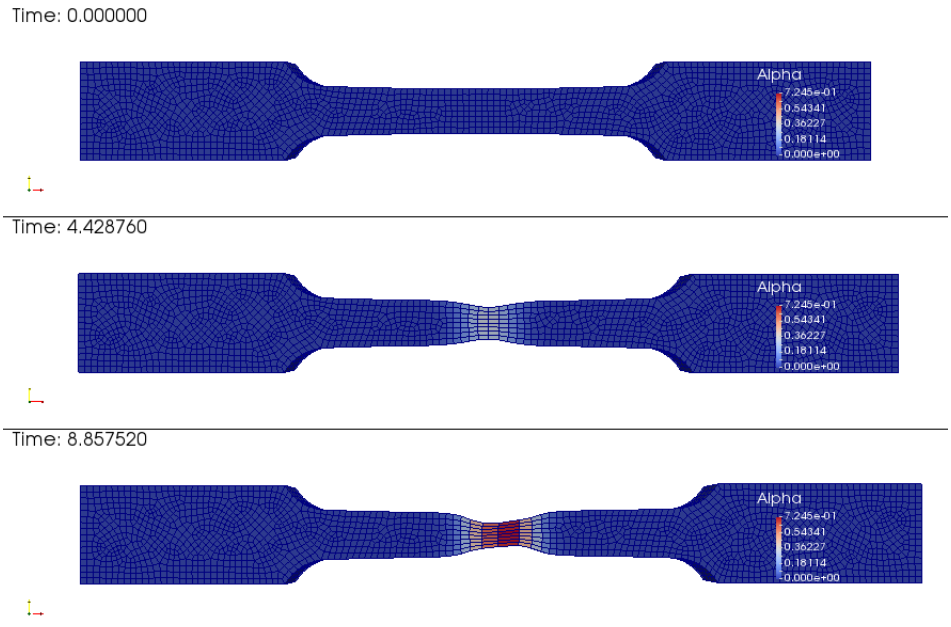

Fig. 12. Plastic strain progression during tensile test

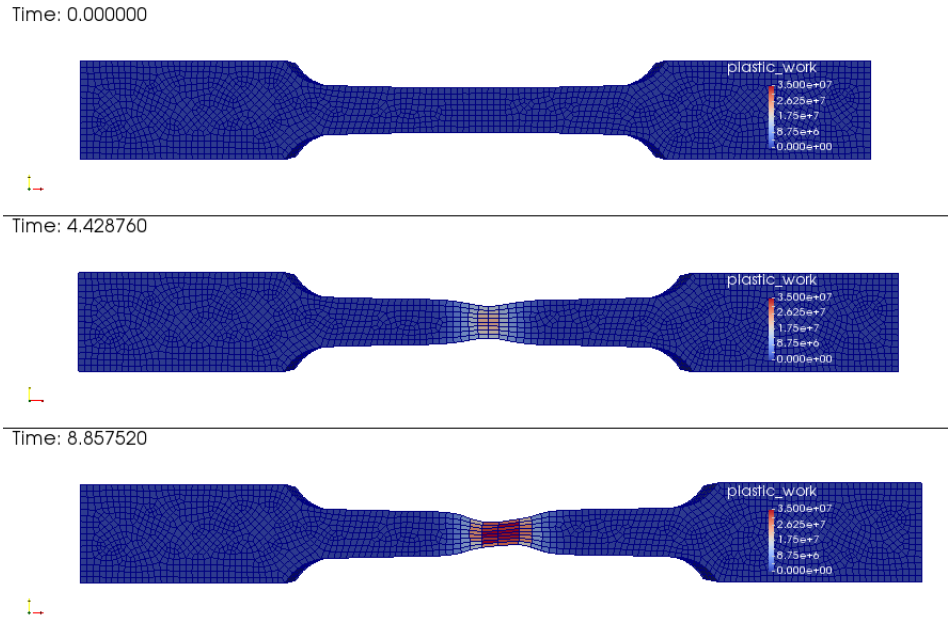

Fig. 13. Plastic work progression during tensile test

4.5 Results and Discussion

The Sandia Fracture Challenge was performed after minor calibration of model parameters. Post-processing capabilities were not sufficient to perform real quantitative comparisons for either the tensile test or the Fracture Challenge. Namely, Paraview does not provide an obvious manner to generate a load displacement curve from which the parameters could be tuned to reproduce the tensile specimen response. Qualitatively, however, the results, shown in Figures 14 and 15 appeared to match well with the experimental results obtained in [15]. The crack path developed in the specimen closely follows the crack path A-C-E (referring to letters in Figure 7) that was apparently due to out-of-tolerance manufacturing. These results were determined to be reasonably successful for a project of this scope.

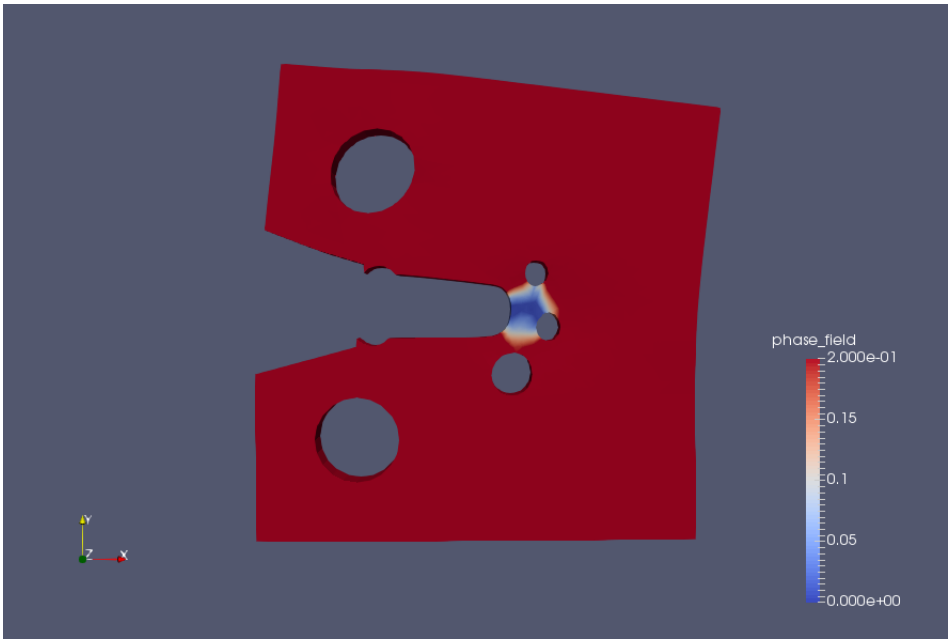

Fig. 14. Phase-field results from the Sandia Fracture Challenge indicate onset of failure where expected

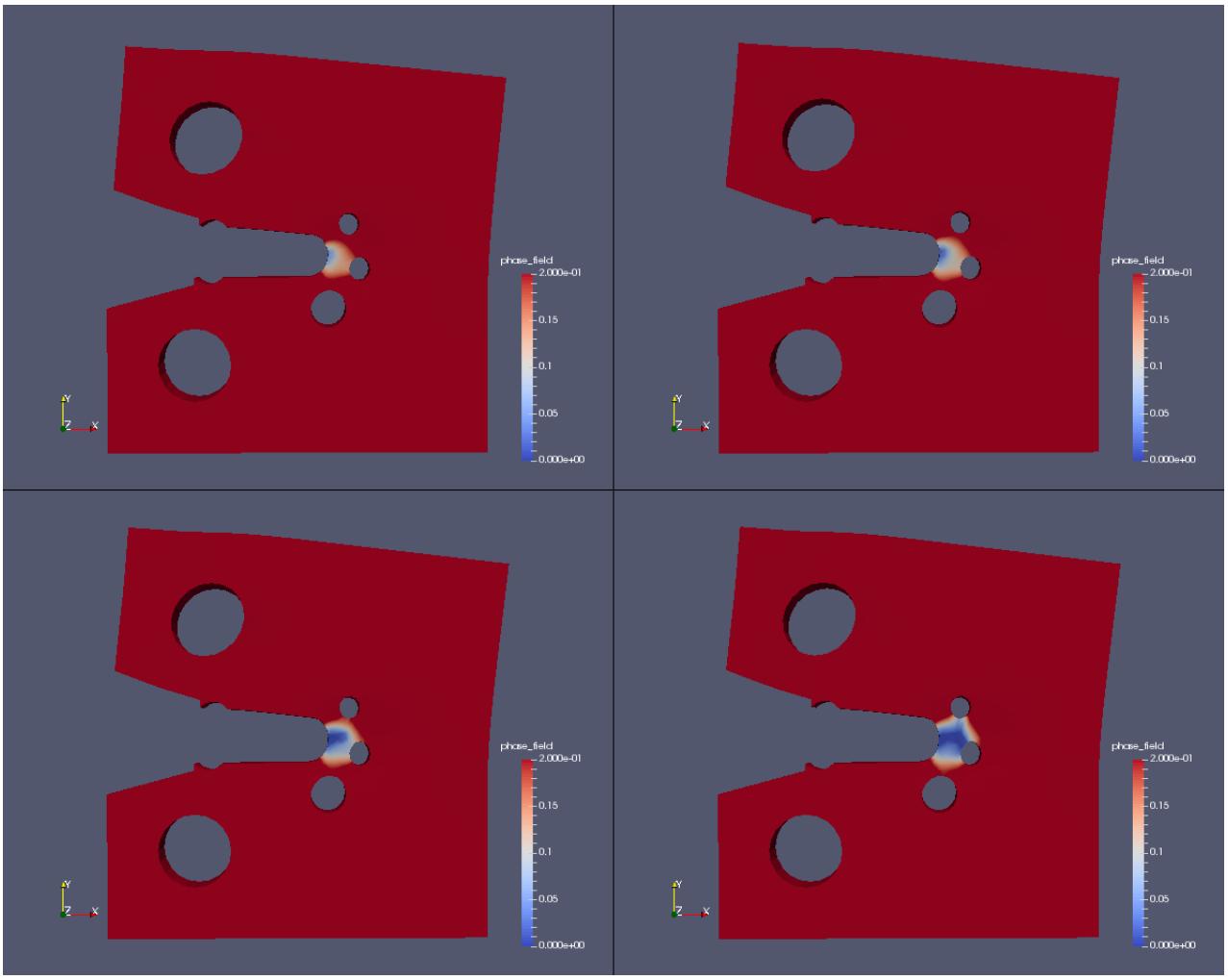

Fig. 15. Damage progression over time

5 Further Discussion and Conclusions

Phase-field fracture techniques have demonstrated their versatility in that they are able to capture the expected modes of fracture for two very dissimilar materials (limestone and stainless steel). The ability to propagate a crack through a material without either needing to specify the initial failure point or accurately track the fracture surface, as well as the generality of the elastic and plastic material response provide compelling reasons why the method should be considered for application to a wide array of problems.

Future work with the coupled model will involve implementing fully integrated solid elements to prevent unwanted spurious solutions. To do this, all 72 variables due to the eight independent quadrature points from each of the nine components of the permeability tensor must be modified at the onset of Poisuille flow. Another means to avoid the hour-glassing phenomena caused by reduced integration is to update the permeability with a continuum approach as outlined in equation (22). By taking this approach, much of the work would be done within the "Phase-Field Porous Flow" material model, avoiding the need to depend on a user subroutine during each time step. Additional validation and verification of the model needs to occur using benchmarks and quantitative comparisons to similar models.

Future work for the elasto-plastic phase-field model would be calibration of the model to the tensile specimens and then further simulation of the Fracture Challenge geometry. Additionally, it would be of interest to perform a mesh convergence/dependence study to see if the fracture path will be unaffected by changes in the mesh. Further still, it would be useful to perform a parameter study to detect the sensitivity of the crack location and load-displacement response to variations in the material parameters. Due to the potential for element entanglement a mesh deletion/failure strategy could also be useful. This might allow the model to run in a more efficient manner.

Sandia National Laboratories is a multimission laboratory managed and operated by National Technology and Engineering Solutions of Sandia, LLC., a wholly owned subsidiary of Honeywell International, Inc., for the U.S. Department of Energy's National Nuclear Security Administration under contract DE-NA0003525.

References

[1] Borden, M. J., Verhoosel, C. V., Scott, M. A., Hughes, T. J., and Landis, C. M., 2012. "A phase-field description of dynamic brittle fracture". *Computer Methods in Applied Mechanics and Engineering,* **217220**, pp. 77 – 95.

[2] Camacho, G., and Ortiz, M., 1996. "Computational modelling of impact damage in brittle materials". *International Journal of Solids and Structures,* **33**(20), pp. 2899 – 2938.

[3] Mos, N., Dolbow, J., and Belytschko, T., 1999. "A finite element method for crack growth without remeshing". *International Journal for Numerical Methods in Engineering,* **46**(1), pp. 131–150.

[4] Silling, S., and Askari, E., 2005. "A meshfree method based on the peridynamic model of solid mechanics". *Computers & Structures,* **83**(1718), pp. 1526 – 1535. Advances in Meshfree Methods.

[5] Foster, J. T., Silling, S. A., and Chen, W. W., 2009. "State based peridynamic modeling of dynamic fracture". pp. 1529–1535.

[6] Bazant, Z., and Y., L., 1995. "Stability of cohesive crack model: Part i– energy principles". *Journal of Applied Mechanics,* **62**(4), pp. 959–964.

[7] Biot, M. A., 1972. Theory of finite deformations of porous solids.

[8] Terzaghi, K., 1925. *Erdbaumechanik auf bodenphysikalischer Grundlage*. F. Deuticke.

[9] Wheeler, M., Wick, T., and Wollner, W., 2014. "An augmented-lagrangian method for the phase-field approach for pressurized fractures". *Computer Methods in Applied Mechanics and Engineering,* **271**, pp. 69 – 85.

[10] Lorentz, E., Cuvilliez, S., and Kazymyrenko, K., 2011. "Convergence of a gradient damage model toward a cohesive zone model". *Comptes Rendus Mcanique,* **339**(1), pp. 20 – 26.

[11] Miehe, C., Hofacker, M., and Welschinger, F., 2010. "A phase field model for rate-independent crack propagation: Robust algorithmic implementation based on operator splits". *Computer Methods in Applied Mechanics and Engineering,* **199**(4548), pp. 2765 – 2778.

[12] Miehe, C., and Mauthe, S., 2015. "Phase field modeling of fracture in multi-physics problems.part iii. crack driving forces in hydro-poro-elasticity and hydraulic fracturing of fluid-saturated porous media". *Comput. Methods Appl. Mech. Engrg,* **304**, pp. 619–655.

[13] Martinez, M., Newell, P., Bishop, J., and Turner, D., 2013. "Coupled multiphase flow and geomechanics model for analysis of joint reactivation during co2 sequestration operations". *International Journal of Greenhouse Gas Control,* **17**, pp. 148–160.

[14] Shaw, R., Agelastos, A. M., and Miller, J. D., 2015. *Guide to Using Sierra*, March.

[15] Boyce, B. L., Kramer, S. L. B., Fang, H. E., Cordova, T. E., Neilsen, M. K., Dion, K., Kaczmarowski, A. K., Karasz, E., Xue, L., Gross, A. J., Ghahremaninezhad, A., Ravi-Chandar, K., Lin, S.-P., Chi, S.-W., Chen, J. S., Yreux, E., Rüter, M., Qian, D., Zhou, Z., Bhamare, S., O'Connor, D. T., Tang, S., Elkhodary, K. I., Zhao, J., Hochhalter, J. D., Cerrone, A. R., Ingraffea, A. R., Wawrzynek, P. A., Carter, B. J., Emery, J. M., Veilleux, M. G., Yang, P., Gan, Y., Zhang, X., Chen, Z., Madenci, E., Kilic, B., Zhang, T., Fang, E., Liu, P., Lua, J., Nahshon, K., Miraglia, M., Cruce, J., DeFrese, R., Moyer, E. T., Brinckmann, S., Quinkert, L., Pack, K., Luo, M., and Wierzbicki, T., 2014. "The sandia fracture challenge: blind round robin predictions of ductile tearing". *International Journal of Fracture,* **186**(1), pp. 5–68.

[16] Bieniawski, Z. T., 1968. "Fracture dynamics of rock". *International Journal of Fracture Mechanics,* **4**(4), pp. 415–430.

[17] Pineau, A., Benzerga, A., and Pardoen, T., 2016. "Failure of metals i: Brittle and ductile fracture". *Acta Materialia,* **107**, pp. 424 – 483.

[18] Borden, M. J., Hughes, T. J., Landis, C. M., Anvari, A., and Lee, I. J., 2016. "A phase-field formulation for fracture in ductile materials: Finite deformation balance law derivation, plastic degradation, and stress triaxiality effects". *Computer Methods in Applied Mechanics and Engineering,* **312**, pp. 130 – 166. Phase Field Approaches to Fracture.